

# Joint Blind Clock Recovery for Space-Division Multiplexed Optical Transmission Systems

Patrick Matalla, *Student Member, IEEE*, Jonas Krimmer, Lennart Schmitz, Dengyang Fang, Christian Koos, and Sebastian Randel, *Senior Member, IEEE*

**Abstract**—In recent years, space-division multiplexing (SDM) has been proposed as a technique to cope with the increasing demand for higher per-fiber capacity in optical networks by modulating multiple independent signals onto multiple spatial paths. This can be accomplished by using specialized fibers that carry multiple signals in a number of fiber cores, fiber modes, or a combination of both types. In such fibers, strong spatial coupling of the signals requires for a joint digital signal processing (DSP) at the receiver. While research has mainly focused on system performance and multiple-input multiple-output (MIMO) equalizers, a reliable joint clock recovery tolerant to spatial-and-polarization-mode dispersion is an active field of research with recent progress. In this paper, we present a novel digital blind joint clock recovery that is tolerant to polarization-and-spatial-mode dispersion. The joint clock recovery is implemented in a feedforward architecture, which allows simple implementation. We provide a detailed analysis of the algorithm complexity for hardware implementation. In simulations, we show low clock phase jitter for fiber lengths up to 10,000 km. Finally, we demonstrate clock recovery for a 90-GBd 16-QAM signal over a 150-km randomly-coupled 4-core fiber (RC-4CF) resulting in a total data rate of 2.88 Tbit/s per wavelength and analyze equalizer convergence using a dedicated joint clock recovery.

**Index Terms**—Space-division multiplexing, optical transmission, multi-core fiber, clock recovery, spatial-and-polarization-mode dispersion.

## I. INTRODUCTION

SPACE-DIVISION MULTIPLEXING (SDM) has become a thriving area of research as it allows to increase the per-fiber information capacity by transmitting independent data signals on multiple spatial paths [1]. In addition, spatial diversity might offer the potential to lower the energy consumption per bit shared hardware. Furthermore, coupled SDM systems benefit from greater tolerance to nonlinearities, the reuse of existing manufacturing, cabling, and installation technologies, and fewer spatial channel outages caused by faulty connectors [2], [3]. On the other hand, coupled SDM systems require a MIMO-DSP which leads to an increased computational complexity [4]. Spatial diversity can be obtained by utilizing multi-core fibers (MCFs), multi-mode fibers (MMFs), or a

combination of both [2], [3]. In MCFs, multiple fiber cores are arranged inside a single fiber cladding. Down to a certain limit of the core pitch where supermodes start to occur, dense packing of the fiber cores leads to strong coupling of the signals [5]. In MMFs, independent signals can be modulated onto the individual spatial modes. Here, modal crosstalk caused, e.g., by fiber imperfections and bends, is leading to a coupling of the signals as well. In both cases, MIMO-DSP at the receiver is indispensable to compensate for the coupled channel impulse response matrix. To leverage the advantages of SDM transceivers, the parallel signals can use a shared oscillator as a clock. In this case, the number of oscillators required is reduced and a joint clock recovery can leverage spatial diversity.

So far, research has mainly focused on system performance and MIMO equalization to mitigate the multidimensional channel impulse response [6], [1]. However, in these experiments, the transmitter and receiver often shared a common clock for best performance, avoiding the need for clock recovery at the receiver [7], [8], [9]. The clock recovery is necessary to either physically synchronize the receiver clock to the transmitter clock in a control loop or to generate a valid flag in case of a free-running receiver clock [10]. This can be achieved by using a joint implementation of an adaptive equalizer with a clock recovery [11], [12]. However, this approach has not been yet been studied in the context of MIMO-equalizers with large dimensions. Furthermore, we show in this work, that a dedicated clock recovery improves the equalizer convergence, which features a significantly increased number of coefficients in SDM systems. While the differential group delay (DGD) in single-core single-mode fibers is still manageably small, it can span multiple tens or hundreds of samples due to spatial-and-polarization-mode dispersion in SDM fibers and, so far, a viable joint clock recovery for coupled SDM channels is still lacking [13], [14].

In our previous work, we demonstrated a joint clock recovery suitable for SDM optical transmission systems with coupled channels [15]. Independently, a similar algorithm has been demonstrated in [16]. Both algorithms rely on the spectral correlation of all received signals, hence, employing the spatial diversity of the signals. In this extended paper, we expand on our research, explain the underlying mathematical concept and provide more detailed simulation results and a complexity analysis. In addition, we investigate the MIMO-equalizer convergence for the three cases of a synchronized transmitter and receiver over a side-channel and non-synchronized transmitter and receiver using only an equalizer-based synchronization as

This work was supported by the German Federal Ministry of Education and Research (in German: Bundesministerium für Bildung und Forschung) in the project STARFALL under Grant 16KIS1420.

P. Matalla, J. Krimmer, L. Schmitz, D. Fang, C. Koos, and S. Randel are with the Institute of Photonics and Quantum Electronics, Karlsruhe Institute of Technology, 76131 Karlsruhe, Germany. (e-mail: patrick.matalla@kit.edu; jonas.krimmer@kit.edu; lennart.schmitz@kit.edu; dengyang.fang@kit.edu; christian.koos@kit.edu; sebastian.randel@kit.edu).

Manuscript received MMMM DD, YYYY; revised MMMM DD, YYYY.

well as dedicated joint clock recovery synchronization. Finally, we have optimized our SDM transmission and demonstrate successful clock synchronization in a 90-GBd 16-level quadrature amplitude modulation (16-QAM) transmission experiment over a 150 km randomly-coupled 4-core fiber (RC-4CF) [17] resulting in a total data rate of 2.88 Tbit/s on a single wavelength.

## II. BLIND JOINT CLOCK RECOVERY

The essential DSP building blocks of our envisioned SDM-receiver are depicted in Fig. 1(a). First, the  $D$  complex-valued, received signals  $r^{(d)}(t)$  are digitized. Here,  $D = 8$  is the number of all coupled spatial degrees of freedom including the polarization and  $d \in \{1, 2, \dots, D\}$ . In addition, we define the number of uncoupled channels as  $K$ , in order to describe uncoupled MCFs, where only the polarizations are coupled, i.e.,  $D = 2$ . For instance, a coupled 4-core fiber has  $D = 8$  and  $K = 1$ , while an uncoupled 4-core fiber has  $D = 2$  and  $K = 4$ . After resampling, a coarse frequency offset compensation is applied as described in [7]. The coarse frequency recovery is applied before the chromatic dispersion (CD) compensation, as we use heterodyne detection in our experiment and hence downconvert the signal to the baseband. For intradyne detection, the frequency recovery can also be performed after blind clock recovery and MIMO equalization as done in common coherent receivers [18]. Afterwards, the quadratic spectral phase caused by CD needs to be removed before the clock recovery. Each signal  $x_k^{(d)}$  at sampling instance  $k$  is then fed into a digital feedforward joint timing estimator to compute a timing estimate  $\hat{\tau} \in [-0.5, 0.5]$  normalized to the symbol period of a sampling offset  $\tau$ . The phase is then unwrapped and divided into an integer sampling offset  $m$  and fractional sampling offset  $\mu \in [0, 1)$  to correct the timing of the delayed signal  $x_k^{(d)}$  in a first-in first-out (FIFO) register used as elastic buffer and a Lagrange interpolator, respectively [19], [20]. In case of a free-running receiver clock, the elastic buffer can under- or overflow and hence a control signal to pause or skip samples is required as explained in [10]. This underlines the necessity of a dedicated clock recovery in asynchronous communication systems. Finally, the signal is fed into a MIMO equalizer. The presented approach does not require a nested architecture of clock recovery and equalization in a feedback loop, which simplifies the implementation.

### A. MIMO Channel Model

The following considerations occur in Fourier domain and the discrete Fourier transform (DFT) of a block of  $N$  samples is denoted by a tilde. We assume, without loss of generality, a signal that is twofold oversampled, i.e., the signal is sampled at a rate of 2 samples per symbol. The  $n$ -th frequency component of the received-signal vector  $\tilde{\mathbf{x}}_n(\tau) \in \mathbb{C}^D$  after propagation through a coupled optical channel can be expressed in terms of the upsampled (sample rate upconversion by inserting zeros in between the symbols) transmit-symbol-sequence vector  $\tilde{\mathbf{s}}_n \in \mathbb{C}^D$  and a lowpass filter  $\tilde{g}_n \geq 0$  applied to the real- and imaginary part of all  $D$  signals that comprises the digital pulse shaping as well as bandwidth limitations of the

transmitter and is assumed to be real-valued and non-negative in frequency-domain (FD) since any nonlinear spectral phase can be compensated in the transmitter DSP. Furthermore, the received signal depends on the baseband MIMO-channel frequency response  $\tilde{\mathbf{H}}_n(\tau) \in \mathbb{C}^D$ , and an additive circularly-symmetric complex-valued Gaussian noise vector  $\tilde{\mathbf{n}}_n$  with distribution  $\mathcal{CN}(\mathbf{0}, \sigma_{\text{noise}}^2 \mathbf{I}^{D \times 1})$  as

$$\tilde{\mathbf{x}}_n(\tau) = \tilde{g}_n \tilde{\mathbf{H}}_n(\tau) \tilde{\mathbf{s}}_n + \tilde{\mathbf{n}}_n. \quad (1)$$

The overall sampling offset  $\tau$  at the receiver is normalized to the symbol period and comprises a mode-averaged group delay of the channel  $\bar{\tau}_{\text{GD}}$ , which we assume to be constant over time, and the time-varying sampling offset  $\tau_{\text{Tx/Rx}}$  between the clocks at the transmitter and receiver side

$$\tau(t) = \tau_{\text{Tx/Rx}}(t) + \bar{\tau}_{\text{GD}}. \quad (2)$$

As we assume a slow drift of the clock phases relative to the DFT size,  $\tau$  can be considered to be constant over time. The objective of the clock recovery is to estimate the transmitter-receiver sampling offset in order to synchronize the sampling phase of the receiver clock to the phase of the transmitter clock. Since  $\tilde{\mathbf{s}}$  is the DFT of an twofold oversampled (by inserting zeros) symbol sequence that consists of i.i.d. random realizations every symbol period from a zero-mean, cyclostationary random process, the Fourier transform  $\tilde{\mathbf{s}}$  is periodic with symbol rate  $N/2$ , i.e.,  $\tilde{\mathbf{s}}_n = \tilde{\mathbf{s}}_{n+N/2}$  for any  $n \in \{1, 2, \dots, N/2\}$ . Hence, the ensemble average  $\langle \cdot \rangle$  of the product of a frequency component at frequency bin  $n$  and the  $N/2$ -separated conjugate transpose component is equal to the variance  $\sigma_s^2$  of the random process

$$\langle \tilde{\mathbf{s}}_n \tilde{\mathbf{s}}_{n+N/2}^\dagger \rangle = \langle \tilde{\mathbf{s}}_n \tilde{\mathbf{s}}_n^\dagger \rangle = \sigma_s^2 \mathbf{I}^{D \times D}. \quad (3)$$

For the sake of simplicity, we neglect any mode-dependent loss (MDL) for now. Using a principal-mode decomposition [21], [22], we factorize the channel matrix as

$$\tilde{\mathbf{H}}_n(\tau) = \tilde{\mathbf{U}} \tilde{\mathbf{D}}_n(\tau) \tilde{\mathbf{V}}^\dagger. \quad (4)$$

In general, the matrices in channel output  $\tilde{\mathbf{U}}$  and channel input  $\tilde{\mathbf{V}}$  express unitary coordinate transformation matrices independent of frequency and  $\tilde{\mathbf{D}}$  is a diagonal matrix that describes the propagation delays  $\tau_d$  of each signal

$$\tilde{\mathbf{D}}_n(\tau) = e^{-j 4\pi \frac{\tau}{N} \mathbf{\Lambda}} \quad (5)$$

with

$$\mathbf{\Lambda} = \text{diag}[\tau_1, \dots, \tau_D] \quad (6)$$

The overall sampling offset can be obtained by calculating the trace of the matrix  $\mathbf{\Lambda}$  as

$$\frac{1}{D} \text{tr}(\mathbf{\Lambda}) = \tau_{\text{Tx/Rx}} + \bar{\tau}_{\text{GD}}. \quad (7)$$

Since we assume a frequency-independent group delay for now,  $\mathbf{\Lambda}$  is independent of frequency. When the spatial channels are uncoupled, the transformation matrices are diagonal matrices and the clock recovery can be applied to all signals individually. In case of coupled signal propagation, modal dispersion (MD) prevents the correct estimation of the clock phase [13], [14]. Using the matrix decomposition, the

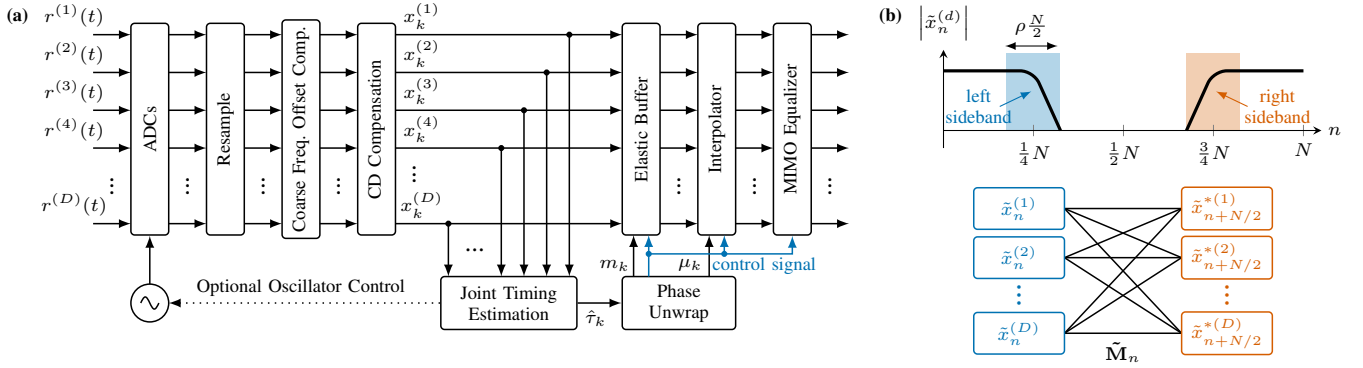


Fig. 1. (a) Multiple-input multiple-output (MIMO) digital signal processing (DSP) building blocks as used in this work for heterodyne detection comprising a joint feedforward clock recovery. (b) shows the spectral magnitude of the  $d$ -th spatial signal, highlighting the overlapping spectral components in the pulse shaping roll-off regions that are contributing to the frequency domain correlation. Below, the multiplication of all left and right sideband components in a butterfly structure and at frequency bin  $n$  resulting in the matrix  $\tilde{\mathbf{M}}_n$  is visualized.

transformation matrices map the transmit and receive signals to the principal modes of the channel which propagate with characteristic group delays [21], [22], [23]. Since the principal modes at the fiber input and output can be different, the unitary matrices  $\tilde{\mathbf{U}}$  and  $\tilde{\mathbf{V}}$  are not identical, see [21]. By considering the delays in the diagonal matrix  $\tilde{\mathbf{D}}_n$ , the sampling offset can be precisely determined.

### B. Joint Timing Estimation Algorithm

In order to apply our channel model from the previous subsection, we consider no residual frequency offset and CD to be fully compensated in the preceding DSP modules (see Fig. 1(a)). Our proposed novel joint timing estimation scheme is based on the algorithm by Barton & Al-Jalili [24], [25], where the phase difference of two frequency components separated by symbol rate is compared to estimate the linear phase that is caused by a time delay in time domain. To do so, a total of  $D$   $N$ -point fast Fourier transforms (FFTs)  $\tilde{\mathbf{x}}(\tau)$  of the received signals are computed. The FFTs are split along the frequency axis into a left and right sideband  $\tilde{\mathbf{x}}_n(\tau)$  and  $\tilde{\mathbf{x}}_{n+N/2}(\tau)$  with  $n = \{1, \dots, N/2\}$ , respectively. Afterwards, we consider a single frequency pair with  $N/2$  frequency separation, which results in a matrix  $\tilde{\mathbf{M}}_n \in \mathbb{C}^{D \times D}$  as

$$\tilde{\mathbf{M}}_n(\tau) = \tilde{\mathbf{x}}_n(\tau) \tilde{\mathbf{x}}_{n+N/2}^\dagger(\tau). \quad (8)$$

Due to the frequency separation equal to the symbol rate, the matrix  $\tilde{\mathbf{M}}$  corresponds to a clock tone at the symbol rate. Considering the ensemble average of  $\tilde{\mathbf{M}}_n$  and inserting the channel model from eq. (1)

$$\begin{aligned} \langle \tilde{\mathbf{M}}_n(\tau) \rangle &= \left\langle \left( \tilde{g}_n \tilde{\mathbf{H}}_n(\tau) \tilde{\mathbf{s}}_n + \tilde{\mathbf{n}}_n \right) \right. \\ &\quad \left. \left( \tilde{g}_{n+N/2} \tilde{\mathbf{s}}_{n+N/2}^\dagger \tilde{\mathbf{H}}_{n+N/2}^\dagger(\tau) + \tilde{\mathbf{n}}_{n+N/2}^\dagger \right) \right\rangle \quad (9) \\ &= \sigma_s^2 \tilde{g}_n \tilde{g}_{n+N/2} \tilde{\mathbf{H}}_n(\tau) \tilde{\mathbf{H}}_{n+N/2}^\dagger(\tau), \end{aligned}$$

where the product of the zero-padded transmit symbol sequence  $\langle \tilde{\mathbf{s}}_n \tilde{\mathbf{s}}_{n+N/2}^\dagger \rangle$  simplifies to the variance  $\sigma_s^2$  and the noise-times-noise and noise-times-signal terms vanish since they

are uncorrelated. Inserting the channel's decomposition from eq. (4) and eq. (5) and defining  $\tilde{\gamma}_n = \tilde{g}_n \tilde{g}_{n+N/2}$  results in

$$\begin{aligned} \langle \tilde{\mathbf{M}}_n(\tau) \rangle &= \sigma_s^2 \tilde{\gamma}_n \tilde{\mathbf{U}} \tilde{\mathbf{D}}_n(\tau) \tilde{\mathbf{V}}^\dagger \tilde{\mathbf{V}} \tilde{\mathbf{D}}_{n+N/2}(\tau) \tilde{\mathbf{U}}^\dagger \\ &= \sigma_s^2 \tilde{\gamma}_n \tilde{\mathbf{U}} e^{-j4\pi \frac{n}{N} \Lambda} e^{j4\pi \frac{n+N/2}{N} \Lambda} \tilde{\mathbf{U}}^\dagger \quad (10) \\ &= \sigma_s^2 \tilde{\gamma}_n \tilde{\mathbf{U}} e^{j2\pi \Lambda} \tilde{\mathbf{U}}^\dagger. \end{aligned}$$

Note that the phase of this expression is frequency-independent. As in the case of polarization mode dispersion (PMD) [26], the determinant removes the influence of the unitary matrix  $\tilde{\mathbf{U}}$ , since  $\det(\tilde{\mathbf{U}} \tilde{\mathbf{U}}^\dagger) = 1$ . The determinant of an diagonal matrix is the product of the diagonal elements. Using eq. (7), this results in

$$\begin{aligned} \det \left( \langle \tilde{\mathbf{M}}_n(\tau) \rangle \right) &= \sigma_s^{2D} \tilde{\gamma}_n^D e^{j2\pi \tau \Lambda} \\ &= \sigma_s^{2D} \tilde{\gamma}_n^D e^{j2\pi D \tau}. \quad (11) \end{aligned}$$

The phase of the determinant is now only proportional to the overall mode-averaged group delay including a constant sampling offset between the transmitter and receiver clock. By computing the argument, i.e., the phase from the interval  $-\pi$  to  $\pi$  of the complex-valued clock tone, the full equation to obtain  $\tau$  is

$$\tau = \frac{1}{2\pi D} \arg \left( \det \left( \langle \tilde{\mathbf{M}}_n(\tau) \rangle \right) \right). \quad (12)$$

In the practical implementation, the ensemble average is approximated as an average over the frequency. Since we are interested in the phase of  $\tilde{\mathbf{M}}_n$ , an averaging over the phase would correspond to the geometric mean

$$\langle \tilde{\mathbf{M}}_n(\tau) \rangle = \left( \prod_{n=1}^{N/2} \tilde{\mathbf{x}}_n(\tau) \tilde{\mathbf{x}}_{n+N/2}^\dagger(\tau) \right)^{\frac{2}{N}}. \quad (13)$$

However, the geometric mean involves many multiplications resulting in a high computational load. To reduce the computational complexity, we approximate the geometric mean using the arithmetic mean. The geometric mean is in good approximation to the arithmetic mean as long as the group delays  $\Lambda$  vary only slightly over the frequency. Averaging over

all  $N/2$  frequency bins, we can approximate eq. (13) using eq. (10) as

$$\begin{aligned} \langle \tilde{\mathbf{M}}_n(\tau) \rangle &\approx \frac{2}{N} \sum_{n=1}^{N/2} \tilde{\mathbf{x}}_n(\tau) \tilde{\mathbf{x}}_{n+N/2}^\dagger(\tau) \\ &= \frac{2}{N} \sum_{n=1}^{N/2} \tilde{\mathbf{M}}_n(\tau) \\ &\approx \sigma_s^2 \tilde{\mathbf{U}} e^{j2\pi\Lambda} \tilde{\mathbf{U}}^\dagger \frac{2}{N} \sum_{n=1}^{N/2} \tilde{\gamma}_n. \end{aligned} \quad (14)$$

We see that the amplitude of the clock tone is affected by the overlapping pulse shape  $\tilde{\gamma}_n$ . As indicated in Fig. 1(b), only the non-zero overlapping areas of the sidebands, which depend on the spectral roll-off of the root-raised cosine (RRC), contribute to the spectral correlation. Hence, only these areas are computed to reduce the computational complexity. The estimation of the sampling offset  $\tau$  is then

$$\hat{\tau} = \frac{1}{2\pi D} \arg \left\{ \det \left( \sum_{\substack{n=1 \\ \tilde{\gamma}_n > 0}}^{N/2} \tilde{\mathbf{x}}_n(\tau) \tilde{\mathbf{x}}_{n+N/2}^\dagger(\tau) \right) \right\}. \quad (15)$$

Note that due to the computation of the argument, the factor  $2/N$  can be omitted. In the case of extreme bandwidth limitations or Nyquist signals (roll-off of approximately 0), modifications similar to those applied to faster-than-Nyquist (FTN) signals are necessary [27], [28], [29]. The modification of the proposed algorithm for such signals is subject of future research activities.

To further reduce the effect of noise on the timing estimate, the spectral correlation  $\tilde{\mathbf{M}} = \sum_n \tilde{\mathbf{M}}_n$  can be averaged over multiple FFT blocks before calculating the determinant. Taking into account the positions of the overlapping areas of the sidebands, the algorithm can also be adapted for fractional oversampling, provided that the signal spectrum can still be resolved [30]. Furthermore, the algorithm is independent on the modulation format. Lastly, note that for one-dimensional signals with  $D = 1$ , e.g., for pulse amplitude modulation, the determinant has the trivial solution  $\det(x) = x$  and hence the proposed algorithm simplifies to the algorithms presented in [19], [25].

### C. Effect of Frequency-Dependent Group Delays

In order to explain the timing estimator approach, we initially neglected any residual CD, MDL, and a frequency-dependence of the group delays in  $\Lambda$  for the sake of simplicity. In general, however, for a modulated signal with a bandwidth that is not small compared to the coherence bandwidth  $1/\sigma_{\text{GD}}$  of the channel, the group delays become frequency-dependent (in [21] also referred to as higher-order MD). This leads to a frequency-dependent group delay  $\tau_{\text{GD},n}^{(d)}$  of the  $d$ -th principal mode and consequently  $\Lambda_n$  [21], [31]. Fig. 2(a) shows the simulated group delays  $\Delta\Lambda_n = \Lambda_n - \Lambda_{n+N/2}$  for all frequency bins from 1 to  $N/2$  and each principal mode of a 4-core fiber with a fiber length of 100 km. We simulated the waveplate model without MDL using 500 segments and

a DGD of  $1\text{ ps}/\sqrt{\text{km}}$  for PMD and a spatial group delay standard deviation  $\sigma_{\text{GD},\text{km}}$  of  $10\text{ ps}/\sqrt{\text{km}}$  [17]. The sampling offset between transmitter and receiver clock is set to zero  $\tau_{\text{Tx/Rx}} = 0$  and no mode-averaged group delay is considered, i.e.,  $\bar{\tau}_{\text{GD},n} = 1/D \text{tr}(\Lambda_n) = 0$ . Fig. 2(a) shows how the respective group delays vary around their mean value with frequency, while the mode-averaged group delay (shown as black dashed line) remains frequency-independent. Due to this property, the geometric mean in eq. (13) can be used for averaging over the frequencies. However, the more hardware-efficient arithmetic mean in eq. (14) produces a good approximation only for a minor frequency dependency. To ensure

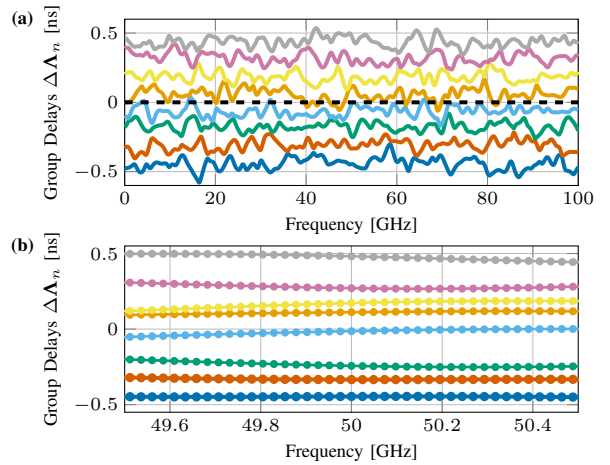


Fig. 2. Simulated group delay  $\Delta\Lambda_n = \Lambda_n - \Lambda_{n+N/2}$  for a 100 km RC-4CF. The waveplate model is emulated by simulating 500 segments with a DGD of  $1\text{ ps}/\sqrt{\text{km}}$  for PMD and a spatial group delay variance  $\sigma_{\text{GD},\text{km}}$  of  $10\text{ ps}/\sqrt{\text{km}}$ . Using a  $2^{13}$ -point FFT, subfigure (a) shows the respective group delays (colored lines) and the mode-averaged group delay (black dashed line) for each frequency bin within 100 GHz, while (b) shows a zoom-in of 1 GHz around the frequency at  $n = N/4$ , that corresponds to 50 GHz for a 100-GbD signal.

that the arithmetic mean delivers a low estimation error, we can adjust the summation limits in eq. (15) to ensure that we are within the coherence bandwidth. This condition is fulfilled for signals with a very low spectral roll-off. For signals with a larger spectral roll-off, the frequency range for averaging must be reduced as the fiber length increases. As a result, the noise suppression deteriorates due to fewer available frequency bins given a fixed FFT size. However, in this case, an averaging of the correlation matrix  $\tilde{\mathbf{M}}$  over several FFT blocks can be applied. For a 100-km-long MCF, the total group delay standard deviation results to  $\sigma_{\text{GD}} = \sqrt{L}\sigma_{\text{GD},\text{km}} = 0.1\text{ ns}$ . The group delay variance of each principal mode, i.e., the elements of  $\Delta\Lambda_n$ , have an averaged variance that is approximately  $\sigma_{\tau_{\text{GD}}^{(d)}}^2 \approx \sigma_{\text{GD}}^2/D$  [21]. This leads to a coherence bandwidth of the group delays of  $\sqrt{D}/\sigma_{\text{GD}} = 28.3\text{ GHz}$ . We consider a bandwidth around  $N/4$  (half the symbol rate, where the roll-off regions overlap, i.e.,  $\tilde{\gamma}_n > 0$ ) that is much smaller than the coherence bandwidth. We find that about 3.5% of the coherence bandwidth (1 GHz) gives a good trade-off between the estimation error of the arithmetic mean and the available number of bins to average over. For a  $2^{13}$ -point FFT, 41 frequency bins are available. The hardware complexity can

be reduced by not implementing the full FFT, but only the relevant frequency components, as explained in section II-D. Fig. 2(b) shows a zoom-in of the group delays  $\Delta\Lambda_n$  within this bandwidth. It can be seen that  $\Delta\Lambda_n$  is only slightly frequency dependent, hence, providing a good approximation of the geometric mean.

#### D. Hardware Complexity Analysis

We analyze the proposed timing estimator complexity for implementation in hardware, e.g., the realization using field-programmable gate arrays (FPGAs) or application-specific integrated circuits (ASICs). We consider the necessity for three real-valued multiplications and three real-valued additions for a complex multiplication and two real-valued additions for a complex addition. Furthermore, we distinguish for a real-valued multiplication between the product of two variable values and the product between a variable and a constant factor, as this can be implemented by a binary shift-add algorithm without the need for dedicated multiplication cells [32]. For the sake of simplicity, we consider signed values (most significant bit (MSB) indicates the sign) with a constant bit width of  $N_{\text{bit}}$  throughout all computations. Therefore, for a multiplication with a constant factor,  $(N_{\text{bit}} - 1)/2$  binary shifts and  $\alpha = (N_{\text{bit}} - 1)/2 - 1$  additions have to be implemented in average for  $N_{\text{bit}} \geq 3$ . For a multiplication with an unknown factor, all possible  $N_{\text{bit}} - 1$  binary shifts must be implemented as well as the entire adder tree, which results in  $\beta = N_{\text{bit}} - 2$  additions.

The complexity  $C$  of the timing estimator is mainly attributed to the  $KD$  FFTs, the complex correlation of the sidebands, the averaging of the correlation, as well as the computation of the determinant. The block size  $N$  of the FFT determines both the frequency resolution and the noise power per frequency component. For a single  $N$ -point split-radix FFT [33], [34], the amount of real-valued operations scale with  $\mathcal{O}(N \log_2(N))$ . In our case, we use a large FFT size because a very low frequency resolution is needed, e.g., when using small pulse shaping roll-off factors (eq. (15)) or to maintain approximate frequency independence (eq. (14)). However, due to the RRC roll-off and the condition of weak frequency dependence, only a very small number of frequency components are used from this large FFT. It is therefore not necessary to implement the entire FFT. Furthermore, a large FFT size of, e.g.,  $2^{13}$ , is not necessary for the averaging of noise given a sufficient signal-to-noise ratio (SNR). For a hardware-efficient implementation, we therefore suggest computing only the necessary frequency components in the range of the pulse shape overlap  $\tilde{\gamma}_n > 0$ . This allows a sufficiently fine choice of frequency resolution, e.g.,  $f_{\text{sa}}/2^{13}$ , but with a smaller averaging length that is in the range of the number of parallel samples per clock cycle, e.g.,  $N = 256$ . Taking into account the DFT symmetry (see Radix-2 FFT [35]), a frequency pair  $\tilde{x}_n$  and  $\tilde{x}_{n+N/2}$  can be computed from a block of  $N$  time-domain samples  $x_k$  with  $k = \{1, 2, \dots, N\}$

as

$$\begin{aligned}\tilde{x}_n &= \sum_{k=0}^{N-1} x_k e^{-j2\pi k \frac{n}{N}} = \tilde{x}_{n,e} + \tilde{x}_{n,o} \\ \tilde{x}_{n+\frac{N}{2}} &= \sum_{k=0}^{N-1} x_k e^{-j2\pi k (\frac{n}{N} + \frac{1}{2})} = \tilde{x}_{n,e} - \tilde{x}_{n,o},\end{aligned}\quad (16)$$

where  $\tilde{x}_{n,e}$  and  $\tilde{x}_{n,o}$  are the even and odd frequency bins of  $\tilde{x}_n$ , respectively. Dividing the incoming time-domain samples  $x_k$  into even  $x_{k,e}$  and odd  $x_{k,o}$  samples in a decimation in time (DIT) unit, the even and odd frequency components can be calculated by

$$\begin{aligned}\tilde{x}_{n,e} &= \sum_{k=0}^{N/2-1} x_{k,e} e^{-j4\pi k \frac{n}{N}} \\ \tilde{x}_{n,o} &= e^{-j2\pi \frac{n}{N}} \sum_{k=0}^{N/2-1} x_{k,o} e^{-j4\pi k \frac{n}{N}}.\end{aligned}\quad (17)$$

The overall block diagram for computing the frequency components as well as the required number of complex operations is shown in Fig. 3(a). As known from the Radix-2 FFT, we can divide the calculation of the frequency components from  $N$  samples into two summations over  $N/2$  samples. These summations each contain four trivial multiplications  $\{-1, 1, -j, j\}$ , so that the total number of complex multiplications is only  $N - 8$ . The required real-valued multiplications  $C_{\text{FC},\times}$  for the so-called twiddle factors and real-valued additions  $C_{\text{FC},+}$  for only one frequency component pair  $\tilde{x}_n$  and  $\tilde{x}_{n+N/2}$  account for

$$\begin{aligned}C_{\text{FC},\times} &= 3N - 21 \\ C_{\text{FC},+} &= 5N - 21.\end{aligned}\quad (18)$$

However, the twiddle factors can be pre-computed and stored in look-up tables (LUTs), and hence, a real-valued multiplication can be realized by using  $\alpha$  additions only. The complexity of  $\nu$  frequency pairs for a total of  $KD$  signals can be expressed only in terms of real-valued additions as

$$C_{\text{FC}} = KD\nu((3\alpha + 5)N - 21(\alpha + 1)). \quad (19)$$

The complexity to compute the frequency components is irrespective of whether the channels are coupled or not and scales linearly with the signal count  $KD$ . The total complexity scales as  $\mathcal{O}(KDN\nu)$ .

The number of complex multiplications and additions of the sidebands depend on the number of frequency pairs  $\nu$  and account for  $D^2\nu$  and  $D^2(\nu - 1)$  operations, respectively. If the spatial channels are not coupled, each pair of polarizations can be processed separately in  $K$   $2 \times 2$  matrices  $\tilde{\mathbf{M}}$ . Hence, the total number of real-valued multiplications and additions is

$$\begin{aligned}C_{\text{corr},\times} &= KD^2 3\nu \\ C_{\text{corr},+} &= KD^2 (5\nu - 2),\end{aligned}\quad (20)$$

As this involves a multiplication of two variable values, the total number of real-valued additions for the correlation results in

$$C_{\text{corr}} = KD^2(3\beta\nu + 5\nu - 2). \quad (21)$$

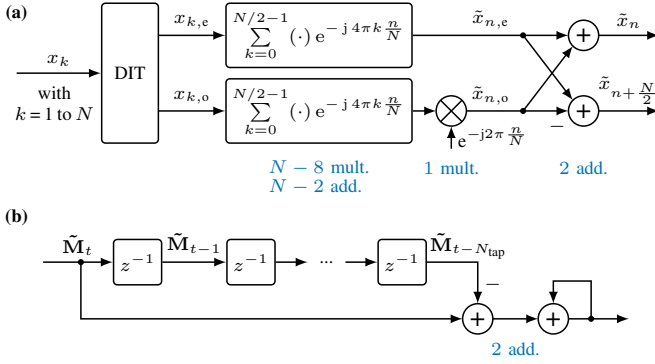


Fig. 3. Hardware architecture for computing the frequency pairs  $\tilde{x}_n$  and  $\tilde{x}_{n+N/2}$  (a) and moving average filter (b). The required complex-valued operations are depicted in blue.

The complexity of the correlation scales quadratically with the number of coupled channels and linearly with the number of frequency pairs as  $\mathcal{O}(KD^2\nu)$ .

The spectral correlation matrix  $\tilde{\mathbf{M}}_t$  at time instance  $t$  is written into a FIFO register and the matrix elements are averaged over consecutive matrices. Using a moving average with simplified architecture as shown in Fig. 3(b), only two complex additions are required for each of the  $D^2$  matrix elements. If the register length is a power of two, the division by the number of filter taps  $N_{\text{tap}}$  is a simple bit truncation. Hence, the total amount of real-valued additions is

$$C_{\text{avg}} = KD^24 \quad (22)$$

and the complexity scales with  $\mathcal{O}(KD^2)$  only.

Finally, the complexity of computing the determinant of a complex matrix is analyzed. The Laplace expansion provides a straightforward implementation for calculating the determinant. However, the complexity scales with  $\mathcal{O}(D!)$ , which makes a hardware implementation even for small matrix dimensions unfeasible [36]. A more common and efficient way to compute the determinant for  $D > 3$  is by using the QR factorization. Here, the complex matrix  $\tilde{\mathbf{M}}$  is decomposed into the product of an orthonormal matrix  $\mathbf{Q}$  and an upper triangular matrix  $\mathbf{R}$  as  $\tilde{\mathbf{M}} = \mathbf{QR}$ . Both matrices can be obtained using the Gram-Schmidt procedure. Because the classical Gram-Schmidt method often produces a matrix  $\mathbf{Q}$  that is not orthonormal, the modified Gram-Schmidt algorithm is used to counteract this issue [37], [38]. Since  $\det(\tilde{\mathbf{M}}) = \det(\mathbf{Q}) \det(\mathbf{R}) = \pm 1 \prod_{i=1}^D r_{i,i}$ , the computation of the determinant mainly consists of the QR factorization and the multiplication of the diagonal complex elements of the matrix  $\mathbf{R}$ . As derived in the Appendix A, the computation of the determinant for  $KD$  signals involves

$$C_{\text{det}} = K \left[ (5 + 3\beta) (D^3 + D^2) + (2 + 3\beta)D - 3\beta - 3 \right] \quad (23)$$

real-valued additions. Compared to the Laplace expansion, the complexity is now reduced and scales with  $\mathcal{O}(KD^3)$ . Finally, the total timing estimation requires  $C = C_{\text{FC}} + C_{\text{avg}} + C_{\text{corr}} + C_{\text{det}}$  real-valued additions. For only a few coupled channels, the complexity is mainly determined by the

frequency components. As the number of coupled channels increases, efficient implementation of the determinant becomes more crucial.

Fig. 4 shows the number of real-valued additions  $C$  per signal required for the clock recovery of  $KD = \{2, 8, 14, 64\}$  signals, e.g., for coupled and uncoupled single-core, 4-core, 7-core, and 32-core fibers. We assume an overall bit width of 6 bit for all calculation steps and neglect bit growth, the computation of  $\nu = 10$  frequency pairs using a block size of  $N = 256$  samples, and an averaging of 8 consecutive correlation matrices. For a coupled 4-core and 32-core fiber, the joint timing estimation requires 9.3% and 336.7% more operations compared to  $K$  clock recovery implementations for individual dual-polarization channels, respectively. However, the algorithm complexity of a joint clock recovery is still low compared to MIMO-equalizers [39]. Finally, we want to emphasize that the use of appropriate FFT sizes also allows joint implementation with FD CD compensation and equalization. Further reduction in FFT complexity could be achieved by splitting a large FFT over several clock cycles such that only a fraction of the total FFT needs to be implemented for each clock cycle [19].

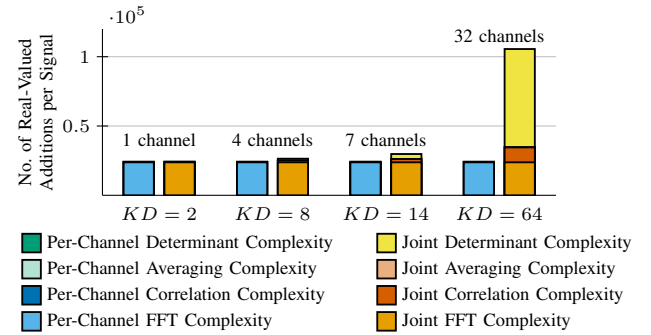


Fig. 4. Number of real-valued additions per signal for  $KD = \{2, 8, 14, 64\}$  signals. The blue/green bars show the complexity for uncoupled spatial channels, i.e.,  $K$  clock recoveries for each dual-polarization signal ( $D = 2$ ) and the red/yellow bars show the complexity for a joint clock recovery employing coupled spatial channels ( $K = 1$ ). The number of operations are computed for a clock recovery with a bit width of 6 bit, 10 frequency pairs, a block size of 256 samples, and averaging of 8 consecutive matrices.

### III. PERFORMANCE SIMULATION

To verify our concept in simulations, we generate a 100-GBd quadrature phase-shift keying (QPSK) sequence, that is twofold oversampled and interpolated using an RRC filter with 0.01 roll-off. Afterwards, we numerically approximate the MCF-channel using the waveplate model [40], [41], [13] with 500 segments and a PMD DGD of  $1 \text{ ps}/\sqrt{\text{km}}$  and an overall spatial channel group delay variance normalized to the square-root fiber length of  $10 \text{ ps}/\sqrt{\text{km}}$  [17]. At the receiver side, additive white Gaussian noise (AWGN) is added to set a certain SNR with a noise bandwidth matching the symbol rate. The resulting signal is filtered using a receive filter matched to the pulse-shaping filter. Finally, the clock recovery algorithm [24] is applied either to each received channel individually or jointly to all received signals using the procedure described in the section before. Fig. 5 shows the simulation results

for a received SNR of 10 dB and a  $2^{13}$ -point FFT of which we compute 11 frequency components per sideband for the timing estimation. Fig. 5(a) shows the timing estimate  $\hat{\tau}$  as a function of the simulated clock phase  $\tau$  obtained for 30,000 signal realizations with constant timing offset  $\tau$  and a single realization of a 3,000 km long 4-core fiber ( $D = 8$ ,  $K = 1$ ). Here, the left and right figure shows the timing estimates without averaging of the correlation matrix  $\tilde{\mathbf{M}}$  and with a moving average of eight consecutive matrices, respectively. It is obvious that the averaging improves the suppression of the random noise, leading to an improvement of jitter from -32 dB to -49 dB. The jitter is defined as the variance of the deviation of the estimated clock phase from the actual clock phase in decibels as  $20 \log_{10}(\text{std}(\hat{\tau} - \tau))$ , where  $\text{std}(\cdot)$  computes the standard deviation. Furthermore, we notice a  $D$ -fold phase ambiguity as expected from eq. (12). Together with the noise, this phase ambiguity can result in errors when unwrapping the phase. However, due to a sufficient large block size  $N$ , the averaging over frequency bins, and optional moving averaging of the correlation matrix  $\tilde{\mathbf{M}}$ , the effect of noise can be effectively reduced.

Each block of  $N$  samples at sample rate  $f_{sa}$  will result to one timing estimate. To further increase the temporal resolution, the sample blocks can overlap by  $N_o$  samples. Finally, the moving average filter will limit the 3-dB bandwidth of the timing estimation to about  $1/N_{\text{tap}}$  of half the estimation rate. The 3-dB bandwidth of the timing estimator  $f_{3\text{dB}}$ , i.e., the maximal frequency of the jitter that can be tracked by the timing estimator, can be expressed as

$$f_{3\text{dB}} \approx \frac{f_{sa}}{N_o} \frac{1}{2N_{\text{tap}}}. \quad (24)$$

Even with a large  $2^{13}$ -point FFT, a clock frequency offset of 5 parts-per-million (ppm) at 200 GSa/s can be resolved by a sufficient number of  $10^6/2^{13}/5 \approx 24$  timing estimations. Considering a practical implementation of single frequency pairs from a block of 256 samples, an overlap of 128 samples, and an averaging of 8 consecutive correlation matrices, the maximum traceable jitter at twofold oversampling results to about 100 MHz, which corresponds to 500 ppm at 200 GSa/s. Note that a feedforward implementation of clock recovery does not require a loop filter in a feedback configuration, which will also feature a lowpass characteristic. This makes the proposed clock recovery architecture applicable for long-haul transmission, where jitter caused by equalization enhanced phase noise may be a limiting factor [42], [43], [44].

Next, we set a constant zero sampling offset  $\tau = 0$  and evaluate the timing jitter from 0 km to 10,000 km. We simulate 1,000 signal realizations for a single MCF channel realization per fiber length from which we compute the jitter. Again, we compute 11 sideband components of a  $2^{13}$ -point FFT and apply an 8-tap moving average of the correlation matrix. In Fig. 5(b), the jitter using a joint clock recovery and a clock recovery applied to each core individually is shown after a simulated MCF transmission with four cores. In addition, we plot as a comparison the joint clock recovery performance for a higher core count of 19 randomly-coupled cores, which we also simulated with a spatial channel group delay variance of

$10 \text{ ps}/\sqrt{\text{km}}$  for a fair comparison to the 4-core fiber and as this was a value experimentally confirmed in [45]. Since the clock recovery for each core after propagating through a 4-core fiber is strongly impaired by MD, the timing estimates are heavily distorted and lie within the gray-shaded area in Fig. 5(b). In contrast to the per-core clock recovery, the joint timing estimation offers low-jitter performance up to a transmission distance of 10,000 km. For the joint clock recovery, we observe a 4-dB and 10-dB degradation for the 4-core and 19-core fiber. The reason for this is a worse approximation of eq. (14) with increasing group delay variance. The 19-core fiber exhibits a better jitter for short fiber distances, since the sampling offset is averaged over a larger matrix. The dashed lines represent a minimum requirement for the jitter in order to prevent distorted timing estimates due to  $D$ -phase ambiguity. They are calculated by assuming an uniform distribution of the timing estimates within the estimation range of  $1/D$  resulting in

$$J_{\text{max}} = 10 \log_{10} \left( \frac{1}{12D^2} \right). \quad (25)$$

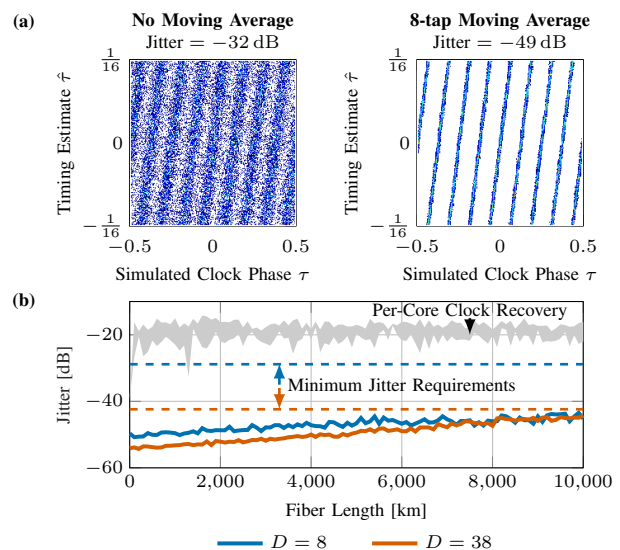


Fig. 5. Clock recovery simulation results for a 1% roll-off QPSK signal with an electrical SNR of 10 dB after propagation through a randomly-coupled multi-core fiber (MCF). (a) Simulated timing estimates  $\hat{\tau}$  over set sampling offset  $\tau$ . The timing estimates are obtained for 30,000 constant timing offset realizations  $\tau$  in a 3,000 km long 4-core fiber ( $D = 8$ ). The left and right figure shows the timing estimates without averaging of the correlation matrix and with an averaging of eight consecutive matrices, respectively. (b) Timing jitter evaluated for 1,000 realizations over fiber length. Using a joint clock recovery with averaging of over eight correlation matrices, the jitter over all 1,000 realizations for a 4-core and 19-core fiber is shown. The jitter for the per-core clock recovery after a 4-core fiber lies within the gray area.

#### IV. EXPERIMENTAL VALIDATION

We validate the joint clock recovery algorithm in an SDM transmission experiment with balanced heterodyne detection, as depicted in Fig. 6. A dual-polarization RRC-shaped 90-GBd 16-QAM signal with 0.01 roll-off factor and sequence length of 230400 i.i.d. symbols, corresponding to  $2.56 \mu\text{s}$ , is generated with a 45-GHz and 120-GSa/s arbitrary waveform

generator (AWG, Keysight M8194A) followed by 50-GHz driver amplifiers (SHF807). Using a 35-GHz dual-polarization inphase and quadrature modulator (DP-IQM), the signal is then modulated onto an optical carrier at 1550 nm generated by an external-cavity laser (ECL) with a nominal linewidth of 100 kHz. The optical signal is amplified by an erbium-doped fiber amplifier (EDFA) and out-of-band amplified spontaneous emission (ASE) noise is suppressed by a 1 nm optical bandpass. Spatial multiplexing is emulated by decorrelating four copies of the signal by delays of 0 ns, 50 ns, 0.5  $\mu$ s, and 1  $\mu$ s (delays determined by fibers available in the lab), respectively, before launching them into the MCF fan-in with an optical signal power of 10 dBm per core. The MCF link consists of three concatenated 50-km-long, single-mode RC-4CF [17] spools, i.e., spanning a total transmission distance of 150 km. The overall group delay spread caused by MD is specified as 10 to 12 ps/ $\sqrt{\text{km}}$ . Including the fan-in and fan-out losses, the total loss per spool is around 9 dB. Therefore, to ensure sufficient optical receive signal power at the photodiodes, the optical signal is amplified to 10 dBm per core after 100 km using four EDFAs. This results in an optical signal power of about 1 dBm per core before the dual-polarization optical hybrids (DP-OHs). At the receiver, a second ECL is used as local oscillator (LO), which is detuned by 48 GHz for balanced heterodyne detection. The LO is amplified before it is split and launched into the four DP-OHs with a power of 17 dBm per receiver. Since we use heterodyne detection, only one quadrature of each signal is detected, and hence, only eight balanced photodiodes (BPDs) and synchronized oscilloscope channels are required. Here, we utilize four 100 GHz BPDs (Fraunhofer HHI) and four 90 GHz BPDs (Finisar BPDV4120R). Finally, 737280 symbols of each received signal are captured by two synchronized 4-channel 100-GHz oscilloscopes (Keysight UXR1004A) and DSP is carried out offline.

The receiver DSP chain is depicted in Fig. 1(a). First, all signals are sampled by analog-to-digital converters (ADCs). Afterwards, the signal is downconverted to baseband and resampled to two samples per symbol. Next, the carrier-frequency offset is estimated from a single polarization and applied to all received signals [7]. After FD CD compensation using the overlap-and-save algorithm [46], our proposed clock recovery follows. The joint clock recovery selects 41 frequency components from each sideband from a  $2^{13}$ -point FFT. In the experiment, we further employ an overlap of  $N/2$  samples for each FFT and average the matrix  $\mathbf{M}$  over 16 consecutive estimates [25]. Afterwards, we use an  $8 \times 8$  MIMO-equalizer with 150 filter taps whose coefficients are obtained using the least mean square (LMS) algorithm with integrated phase recovery switching from data-aided to decision-directed mode [6] after 40,000 computed output symbols. To achieve fast convergence in the initialization phase and improved convergence later, the stochastic gradient descent step size is switched from  $\mu_1 = 5 \times 10^{-5}$  to a step size  $\mu_2$  after 20,000 computed output symbols. After the MIMO-equalizer, we use a real-valued  $2 \times 2$  post-equalizer for each received polarization to remove residual transmitter impairments. Lastly, we evaluate the bit error ratio (BER) and the signal-to-noise-and-distortion ratio (SNDR) over the final

$5 \times 10^5$  symbols.

To prove the proper operation of our approach, we use the AWG and oscilloscopes with and without external synchronization through a side channel. Fig. 7(a) shows successful timing estimation for both cases over 8  $\mu$ s. We can observe a frequency offset of about 880 kHz between the transmitter and receiver, that corresponds to around 4.9 ppm at twofold oversampling. Without dedicated clock recovery, the MIMO-equalizer would have to continuously track and compensate this sampling phase walk. This becomes apparent in Fig. 7(b), where the equalizer convergence is examined. The figure shows the temporal evolution of the LMS error, which is smoothed over time and averaged for all  $D = 8$  signals. Here, the equalizer is operated in data-aided mode only. For the case of a synchronized transmitter and receiver, the equalizer must mainly compensate for a constant sampling offset with weak phase fluctuations (see orange line in Fig. 7(a)), which is why it still converges reliably for a low step size of  $\mu_2 = 5 \times 10^{-6}$ . In the scenario where transmitter and receiver are not synchronized and no clock recovery is used (see blue curves in Fig. 7(a)), the equalizer must also track and compensate for a clock frequency offset. In this case, the feedback control loop of the equalizer must have the necessary bandwidth and stability. Note, that the step size  $\mu$  corresponds to the integral coefficient in a phase-locked loop (PLL) design. For a low step size of  $\mu_2 = 5 \times 10^{-6}$ , the LMS error increases in the second training phase since the equalizer cannot follow the clock phase drift fast enough. For this reason,  $\mu_2$  has to be set to a larger value to follow the 4.9 ppm clock phase drift. In this case, the equalizer performs comparably to the case of a synchronized transmitter and receiver. In the realistic scenario, with no synchronization but with dedicated clock recovery, the LMS error is about 1 dB lower. In this case, the equalizer only has to compensate for a constant sampling offset, but no clock phase fluctuations, i.e., it has to track reduced channel dynamics. This allows for a small step size parameter  $\mu_2$  and enables a better convergence as well as an improved stability of the equalizer. It should be emphasized that the equalizer convergence significantly affects the performance when switching to hard-decision mode, as this causes a worse LMS error the more errors are made during decisioning.

The transmission performance in terms of the SNDR and BER for all 8 signals and no synchronization between transmitter and receiver is shown in Fig. 7(c). The results shown in gray ( $\mu_2 = 5 \times 10^{-5}$ ) and blue ( $\mu_2 = 5 \times 10^{-6}$ ) are for the case without and with dedicated clock recovery, respectively. The results with joint clock recovery are for the hard-decision mode, while for the equalizer-based clock recovery the data-aided mode was applied, as too many errors in the hard-decision caused the equalizer to diverge. For the SNDR, we observe an improvement of 1 dB if our proposed joint clock recovery is used. We demonstrate successful transmission assuming a pre-forward error correction (FEC) BER limit of  $2.41 \times 10^{-2}$ , which can in principle be achieved, e.g., using a soft-decision LDPC code with 20% overhead [47], [48].

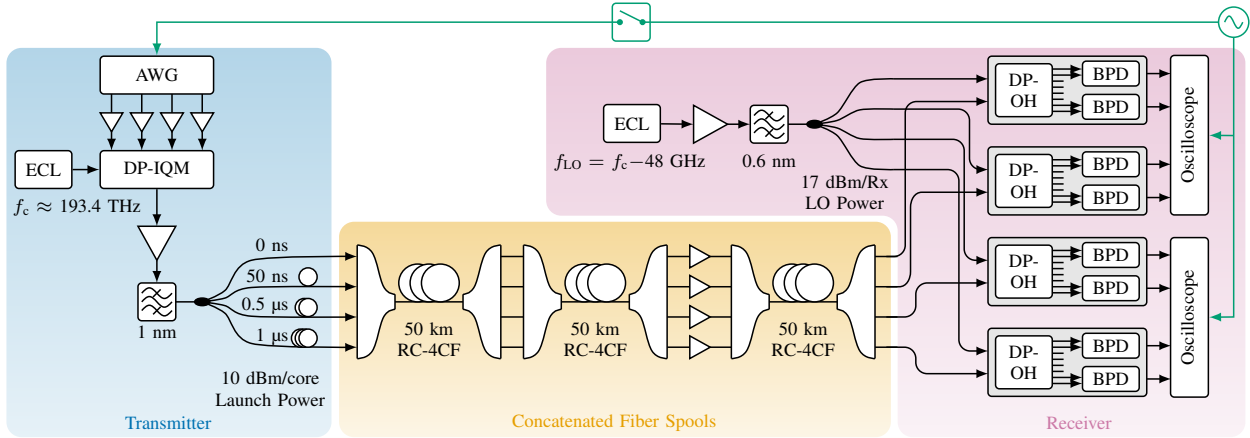


Fig. 6. 150 km randomly-coupled 4-core fiber (RC-4CF) transmission setup employing balanced heterodyne detection. Synchronization between the transmitter and receiver can be obtained using a side channel with a switch (green).

## V. CONCLUSIONS AND OUTLOOK

We have presented a novel joint clock recovery algorithm that is tolerant to spatial-and-polarization-mode dispersion by computing the joint group delays of the principal modes in FD from the spectral correlation matrix. In simulations, the algorithm performs well for randomly-coupled fibers with lengths of up to 10,000 km. Furthermore, we analyzed the hardware complexity for FPGA or ASIC implementation. Compared to uncoupled-channel dual-polarization signals, computing the determinant of large correlation matrices becomes more crucial. Finally, we experimentally demonstrated joint clock recovery in a 90-GBd 16-QAM transmission over 150 km RC-4CF resulting in a total data rate of 2.88 Tbit/s. Using a dedicated clock recovery relieves the equalizer and improves equalizer convergence and stability, which results in an SNDR improvement by more than 1 dB in hard-decision mode. More in-depth research regarding the effect of a frequency-dependent mode-averaged group delay and the influence of mode-dependent loss as well as optimizations for improved inphase and quadrature imbalance tolerance is proposed for future research. The dispersion-tolerant clock recovery algorithm presented in this work enables robust and hardware-efficient DSP in future SDM systems and is an important step towards the practical use of SDM systems.

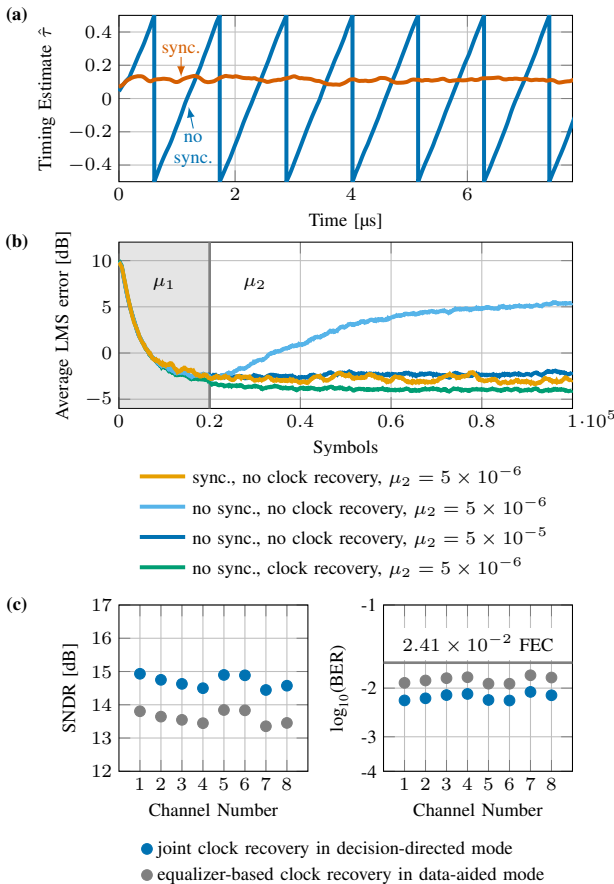


Fig. 7. (a) Timing-error evolution (modulo one symbol interval) with and without external synchronization of the transmitter and receiver. (b) Least mean square (LMS) error smoothed over time and averaged over all receive signals over the number of computed output symbols. (c) Signal-to-noise-and-distortion ratio (SNDR) and bit error ratio (BER) for all eight receive signals.

## APPENDIX A

### DETERMINANT COMPLEXITY USING THE MODIFIED GRAM-SCHMIDT FACTORIZATION

The modified Gram-Schmidt factorization is a common way to implement the QR factorization on hardware [37], [38]. By QR factorizing the matrix  $\tilde{\mathbf{M}} = \mathbf{Q}\mathbf{R}$  into an orthonormal matrix  $\mathbf{Q}$  and an upper triangular matrix  $\mathbf{R}$ , the calculation of the determinant can be simplified, since  $\det(\tilde{\mathbf{M}}) = \det(\mathbf{Q})\det(\mathbf{R}) = \pm 1 \prod_{i=1}^D r_{i,i}$ . Algorithm 1 shows the procedure to find  $\mathbf{Q}$  and  $\mathbf{R}$  with the required number of complex operations given as comments.

With  $\sum_{k=1}^D k = D(D+1)/2$  we find the number of complex multiplications and additions required for the QR

---

**Algorithm 1: Gram-Schmidt Factorization**

---

```

 $\tilde{\mathbf{M}}$ :  $D \times D$  Spectral correlation matrix
 $\mathbf{Q} = \tilde{\mathbf{M}}$ 
 $\mathbf{R} = \mathbf{I}$ 
// D times
for  $i = 1$  to  $D$  do
     $r_{i,i} = \text{sqrt}(\mathbf{q}_{:,i}^\dagger \mathbf{q}_{:,i})$  // D squares, D-1 add.
     $\mathbf{q}_{:,i} = \mathbf{q}_{:,i} / r_{i,i}$  // D divisions
    // D-1 times
    for  $j = i + 1$  to  $D$  do
         $r_{i,j} = \mathbf{q}_{:,j}^\dagger \mathbf{q}_{:,i}$  // D mult., D-1 additions
         $\mathbf{q}_{:,j} = \mathbf{q}_{:,j} - r_{i,j} \mathbf{q}_{:,i}$  // D subtr., D mult.
    end
end
end

```

---

factorization to be

$$\begin{aligned}
 C_{\text{det,comp.}\times} &= \sum_{k=1}^D 2D + 2D(D - k) \\
 &= D^3 + D^2 \\
 C_{\text{det,comp.}+} &= \sum_{k=1}^D D - 1 + (D - k)(2D - 1) \\
 &= D^3 - \frac{1}{2}D^2 - \frac{1}{2}D.
 \end{aligned} \tag{26}$$

After QR factorization, the determinant is mainly given by the product of the diagonal elements in  $\mathbf{R}$ , which involves  $D - 1$  additional complex multiplications. This gives

$$\begin{aligned}
 C_{\text{det},\times} &= 3D^3 + 3D^2 + 3D - 3 \\
 C_{\text{det},+} &= 5D^3 + 5D^2 + 2D - 3.
 \end{aligned} \tag{27}$$

real-valued multiplications and additions and finally leads to eq. (23) considering the multiplications realized using the shift-add algorithm.

REFERENCES

- [1] B. J. Puttnam, G. Rademacher, and R. S. Luís, "Space-division multiplexing for optical fiber communications," *Optica*, vol. 8, no. 9, pp. 1186–1203, Sep. 2021.
- [2] G. Rademacher, B. Puttnam, R. Luís, T. Eriksson, N. Fontaine, M. Mazur, H. Chen, R. Ryf, D. Neilson, P. Sillard, F. Achten, Y. Awaji, and H. Furukawa, "Peta-bit-per-second optical communications system using a standard cladding diameter 15-mode fiber," *Nat. Commun.*, vol. 12, p. 4238, July 2021.
- [3] T. Matsui, P. L. Pondillo, and K. Nakajima, "Weakly coupled multicore fiber technology, deployment, and systems," *Proc. IEEE*, vol. 110, no. 11, pp. 1772–1785, Nov. 2022.
- [4] P. J. Winzer and D. T. Neilson, "From scaling disparities to integrated parallelism: A decathlon for a decade," *J. Lightw. Technol.*, vol. 35, no. 5, pp. 1099–1115, Mar. 2017.
- [5] T. Hayashi, T. Sakamoto, Y. Yamada, R. Ryf, R.-J. Essiambre, N. Fontaine, M. Mazur, H. Chen, and T. Hasegawa, "Randomly-coupled multi-core fiber technology," *Proc. IEEE*, vol. 110, no. 11, pp. 1786–1803, Nov. 2022.
- [6] S. Randel, R. Ryf, A. Sierra, P. J. Winzer, A. H. Gnauck, C. A. Bolle, R.-J. Essiambre, D. W. Peckham, A. McCurdy, and R. Lingle, "6x56-Gb/s mode-division multiplexed transmission over 33-km few-mode fiber enabled by 6x6 MIMO equalization," *Opt. Express*, vol. 19, no. 17, pp. 16 697–16 707, Aug. 2011.
- [7] M. van den Hout, "Ultra-wideband and space-division multiplexed optical transmission systems," Ph.D. dissertation, Eindhoven University of Technology, 2024.
- [8] M. Mazur, R. Ryf, N. K. Fontaine, A. Marotta, E. Börjeson, L. Dallachiesa, H. Chen, T. Hayashi, T. Nagashima, T. Nakanishi, T. Morishima, F. Graziosi, L. Palmieri, D. T. Neilson, P. Larsson-Edefors, A. Mecozzi, and C. Antonelli, "Real-time MIMO transmission over field-deployed coupled-core multi-core fibers," in *Proc. Opt. Fiber Commun. Conf.*, Mar. 2022, paper Th4A.1.
- [9] M. Mazur, L. Dallachiesa, N. K. Fontaine, R. Ryf, E. Börjeson, H. Chen, H. Sakuma, T. Ohtsuka, T. Hayashi, T. Hasegawa, H. Tazawa, D. T. Neilson, and P. Larsson-Edefors, "Real-time transmission over 2x55 km all 7-core coupled-core multi-core fiber link," in *Proc. Opt. Fiber Commun. Conf.*, Mar. 2022, paper Th4A.1.
- [10] D. Schmidt and B. Lankl, "Parallel architecture of an all digital timing recovery scheme for high speed receivers," in *2010 7th International Symposium on Communication Systems, Networks & Digital Signal Processing (CSNDSP 2010)*, July 2010, pp. 31–34.
- [11] K. Kikuchi, "Clock recovering characteristics of adaptive finite-impulse-response filters in digital coherent optical receivers," *Opt. Express*, vol. 19, no. 6, pp. 5611–5619, Mar. 2011.
- [12] M. Kuschnerov, F. Hauske, K. Piyawanno, B. Spinnler, E.-D. Schmidt, and B. Lankl, "Joint equalization and timing recovery for coherent fiber optic receivers," in *Proc. Eur. Conf. Opt. Commun.*, Sep. 2008, paper Mo.3.D.3, pp. 1–2.
- [13] J. C. M. Diniz, F. Da Ros, and D. Zibar, "Clock recovery challenges in DSP-based coherent single-mode and multi-mode optical systems," *Future Internet*, vol. 10, no. 7, June 2018.
- [14] D. Wang, M. Qiao, K. Lian, and Z. Li, "CD and PMD effect on cyclostationarity-based timing recovery for optical coherent receivers," *J. Lightw. Technol.*, vol. 41, no. 8, pp. 2405–2412, Apr. 2023.
- [15] P. Matalla, L. Schmitz, J. Krimmer, D. Fang, C. Koos, and S. Randel, "Demonstration of joint blind clock recovery in a 1.92 Tbit/s transmission over 50 km randomly-coupled 4-core fiber," in *Proc. Eur. Conf. Opt. Commun.*, Sep. 2024, paper W4C.6.
- [16] M. Qiao, Y. Wang, Z. Li, Y. Xiao, Y. Chen, Z. Li, and D. Wang, "Novel dispersion and timing estimation for weakly-coupled OAM fiber transmission systems," *IEEE Photon. Technol. Lett.*, vol. 36, no. 14, pp. 913–916, June 2024.
- [17] T. Hayashi, Y. Tamura, T. Hasegawa, and T. Taru, "Record-low spatial mode dispersion and ultra-low loss coupled multi-core fiber for ultra-long-haul transmission," *J. Lightw. Technol.*, vol. 35, no. 3, pp. 450–457, Feb. 2017.
- [18] S. J. Savory, "Digital coherent optical receivers: Algorithms and sub-systems," *IEEE J. Sel. Topics Quantum Electron.*, vol. 16, no. 5, pp. 1164–1179, 2010.
- [19] P. Matalla, M. S. Mahmud, C. Füllner, C. Koos, W. Freude, and S. Randel, "Hardware comparison of feed-forward clock recovery algorithms for optical communications," in *Proc. Opt. Fiber Commun. Conf.*, June 2021, paper Th1A.10, pp. 1–3.
- [20] C. Fludger, T. Duthel, P. Hermann, and T. Kupfer, "Jitter tolerant clock recovery for coherent optical receivers," in *Proc. Opt. Fiber Commun. Conf.*, Mar. 2013, paper OTh1F.3, pp. 1–3.
- [21] K.-P. Ho and J. M. Kahn, "Chapter 11 - mode coupling and its impact on spatially multiplexed systems," in *Optical Fiber Telecommunications (Sixth Edition)*, sixth edition ed., ser. Optics and Photonics, I. P. Kaminow, T. Li, and A. E. Willner, Eds. Boston: Academic Press, 2013, pp. 491–568.
- [22] E. Deriushkina, J. Schröder, and M. Karlsson, "Dynamic model for coupled-core fibers," *J. Lightw. Technol.*, pp. 1–9, July 2024.
- [23] J. Carpenter, B. J. Eggleton, and J. Schröder, "Comparison of principal modes and spatial eigenmodes in multimode optical fibre," *Laser Photonics Rev.*, vol. 11, no. 1, p. 1600259, Dec. 2016.
- [24] S. Barton and Y. Al-Jalili, "A symbol timing recovery scheme based on spectral redundancy," in *IEE Colloquium on Advanced Modulation and Coding Techniques for Satellite Communications*, Jan. 1992, pp. 3/1–3/6.
- [25] P. Matalla, M. S. Mahmud, C. Koos, and S. Randel, "Pilot-free digital clock synchronization for continuous-variable quantum key distribution," in *Proc. Eur. Conf. Opt. Commun.*, Oct. 2023, pp. 1386–1389.
- [26] N. Kaneda, A. B. Leven, and S. Weisser, "Symbol timing recovery in polarization division multiplexed coherent optical transmission system," U.S. Patent US 8,655,191 B2, Feb., 2014.
- [27] K.-T. Wu and H. Sun, "Frequency-domain clock phase detector for Nyquist WDM systems," in *Proc. Opt. Fiber Commun. Conf.*, Mar. 2014, paper Th3E.2, pp. 1–3.

- [28] M. Yan, Z. Tao, L. Dou, L. Li, Y. Zhao, T. Hoshida, and J. C. Rasmussen, "Digital clock recovery algorithm for Nyquist signal," in *Proc. Opt. Fiber Commun. Conf.*, Mar. 2013, paper OTu21.7, pp. 1–3.
- [29] N. Stojanovic, B. Mao, and Y. Zhao, "Digital phase detector for Nyquist and faster than Nyquist systems," *IEEE Commun. Lett.*, vol. 18, no. 3, pp. 511–514, Apr. 2014.
- [30] A. Josten, B. Baeuerle, E. Dornbierer, J. Boesser, D. Hillerkuss, and J. Leuthold, "Modified Godard timing recovery for non integer oversampling receivers," *Appl. Sci.*, vol. 7, no. 7, June 2017.
- [31] M. Cappelletti, M. Mazur, N. K. Fontaine, R. Ryf, T. Hayashi, A. Mecozzi, M. Santagiustina, A. Galtarossa, C. Antonelli, and L. Palmieri, "Statistical analysis of modal dispersion in field-installed coupled-core fiber link," *J. Lightw. Technol.*, vol. 42, no. 11, pp. 4103–4109, June 2024.
- [32] U. Meyer-Baese, *Digital Signal Processing with Field Programmable Gate Arrays*, 4th ed. Springer Publishing Company, Incorporated, 2014.
- [33] R. Yavne, "An economical method for calculating the discrete Fourier transform," in *Fall Joint Computer Conference*, ser. AFIPS '68 (Fall, part I). New York, NY, USA: Association for Computing Machinery, Dec. 1968, p. 115–125.
- [34] P. Duhamel and H. Hollmann, "'split radix' FFT algorithm," *Electron. Lett.*, vol. 20, pp. 14 – 16, Jan. 1984.
- [35] J. W. Cooley and J. W. Tukey, "An algorithm for the machine calculation of complex Fourier series," *Mathematics of Computation*, vol. 19, pp. 297–301, 1965.
- [36] H. E. Rose, *Linear Algebra: A Pure Mathematical Approach*. Birkhäuser Verlag, 2002.
- [37] Å. Björck, "Numerics of gram-schmidt orthogonalization," *Linear Algebra and its Applications*, vol. 197–198, pp. 297–316, Apr. 1994.
- [38] G. Rünger and M. Schwind, "Comparison of different parallel modified Gram-Schmidt algorithms," in *International European Conference on Parallel and Distributed Computing*. Springer Berlin Heidelberg, 2005, pp. 826–836.
- [39] S. Randel, P. J. Winzer, M. Montoliu, and R. Ryf, "Complexity analysis of adaptive frequency-domain equalization for MIMO-SDM transmission," in *Proc. Eur. Conf. Opt. Commun.*, Sep. 2013, pp. 1–3.
- [40] J.-P. Elbers, C. Glingener, M. Duser, and E. Voges, "Modelling of polarisation mode dispersion in singlemode fibres," *Electron. Lett.*, vol. 33, pp. 1894 – 1895, Nov. 1997.
- [41] J. P. Gordon and H. Kogelnik, "PMD fundamentals: Polarization mode dispersion in optical fibers," *Proc. Natl. Acad. Sci.*, vol. 97, no. 9, pp. 4541–4550, Apr. 2000.
- [42] H. Sun and K.-T. Wu, "Clock recovery and jitter sources in coherent transmission systems," in *Proc. Opt. Fiber Commun. Conf.*, Mar. 2012, paper OTh4C.1, pp. 1–3.
- [43] C. S. Martins, A. Llorens-Riesgo, S. Mumtaz, T. H. Nguyen, A. Hraghi, Z. Wu, Y. Frignac, G. Charlet, and Y. Zhao, "Frequency-band analysis of equalization enhanced phase noise jointly with DSP impact," in *Proc. Opt. Fiber Commun. Conf.*, Mar. 2024, paper Tu2H.5, pp. 1–3.
- [44] M. Qui, X. Tang, Y. Chen, J. He, and C. Li, "Mitigation of equalization enhanced phase noise using feedforward timing error correction," in *Proc. Eur. Conf. Opt. Commun.*, Sep. 2024, paper W4C.2.
- [45] G. Rademacher, M. van den Hout, R. S. Luís, B. J. Puttnam, G. Di Sciullo, T. Hayashi, A. Inoue, T. Nagashima, S. Gross, A. Ross-Adams, M. J. Withford, J. Sakaguchi, C. Antonelli, C. Okonkwo, and H. Furukawa, "Randomly coupled 19-core multi-core fiber with standard cladding diameter," in *Proc. Opt. Fiber Commun. Conf.*, Mar. 2023, paper Th4A.4, pp. 1–3.
- [46] T. Xu, G. Jacobsen, S. Popov, M. Forzati, J. Mårtensson, M. Mussolin, J. Li, K. Wang, Y. Zhang, and A. T. Friberg, "Frequency-domain chromatic dispersion equalization using overlap-add methods in coherent optical system," *J. Opt. Commun.*, vol. 32, no. 2, pp. 131–135, June 2011.
- [47] D. A. Morero, M. A. Castrillon, F. A. Ramos, T. A. Goette, O. E. Agazzi, and M. R. Hueda, "Non-concatenated FEC codes for ultra-high speed optical transport networks," in *IEEE Global Telecommunications Conference*, Dec. 2011, pp. 1–5.
- [48] H. Li and L. Schmalen, "A spatially coupled LDPC coding scheme with scalable decoders for space division multiplexing," in *Proc. Eur. Conf. Opt. Commun.*, Oct. 2023, p. 1186 – 1189.



**Patrick Matalla** (Student Member, IEEE) received his B.Sc. and M.Sc. degrees in electrical engineering from the Karlsruhe Institute of Technology (KIT), Karlsruhe, Germany, in 2018 and 2020, respectively. He joined the Institute of Photonics and Quantum Electronics (IPQ) at KIT in 2020, where he is currently working towards his Ph.D. His research interests include digital signal processing in optical communication systems and the algorithm hardware implementation on field-programmable gate arrays (FPGAs).



**Jonas Krimmer** earned his B.Sc. and M.Sc. degrees in electrical engineering from the Karlsruhe Institute of Technology (KIT) in Karlsruhe, Germany, in 2017 and 2020, respectively. In 2020, he joined the Institute of Photonics and Quantum Electronics (IPQ) at KIT, where he is currently pursuing his Ph.D. His research interests include free-space optical communications, space-division multiplexing, and digital signal processing for optical communications.



**Lennart Schmitz** received his B.Sc. and M.Sc. degrees in electrical engineering from the Karlsruhe Institute of Technology (KIT), Karlsruhe, Germany, in 2021 and 2024, respectively. He joined the Institute of Photonics and Quantum Electronics (IPQ) at KIT in 2024, where he is currently working towards his Ph.D. His research interests include digital signal processing in optical communication systems and photonic-electronic systems for ultra-broadband optical arbitrary waveform generation and measurement.



**Dengyang Fang** received the B.Sc. degree in Physics from East China Normal University (ECNU), Shanghai, China, in 2014 and the M.Sc. degree in Physics from Karlsruhe Institute of Technology (KIT), Karlsruhe, Germany, in 2018. Since 2019, he has been working towards the Ph.D. degree in electrical engineering at the Institute of Photonics and Quantum Electronics (IPQ) at KIT. His research interests include developing optical frequency comb-based photonic-electronic systems for ultra-broadband optical arbitrary waveform generation and measurement, analogue-to-digital conversion, as well as their implementation on integrated photonic chips.



**Christian Koos** received the Ph.D. (Dr.-Ing.) degree in electrical engineering from the University of Karlsruhe, Karlsruhe, Germany, in 2007. He is currently a full Professor with the Karlsruhe Institute of Technology, Karlsruhe, Germany, where he is heading the Institute of Photonics and Quantum Electronics. He has co-founded several start-up companies, such as Vanguard Photonics GmbH, Vanguard Automation GmbH, SilOriX GmbH, and DeepLight SA. From 2008 to 2010, he was affiliated with the Corporate Research and Technology Department of Carl Zeiss

AG in Oberkochen, Germany, where he led the technology forecast in the area of nanotechnology. He is the author of more than 140 journal papers and more than 30 patent families. His research interests include silicon photonics and hybrid integration concepts along with the associated applications in high-speed communications, optical sensing and metrology, and ultra-fast photonic-electronic signal processing. He was the recipient of several research awards and prestigious grants, such as the ERC Starting Grant in 2011 and ERC Consolidator Grant in 2017.



**Sebastian Randel** (Senior Member, IEEE) received his Dr.-Ing. degree in 2005 from Technische Universität Berlin, Germany, for his work on high-speed optical-time-division-multiplexed transmission systems. Since 2016, he has been a full Professor at the Karlsruhe Institute of Technology (KIT), Karlsruhe, Germany, where he co-heads the Institute of Photonics and Quantum Electronics. From 2005 to 2010, he was a Research Scientist at Siemens Corporate Technology, Munich, Germany, leading research and standardization activities in polymer-

optical-fiber communications, visible light communications, and optical access networks. From 2010 to 2016, he served as a Member of Technical Staff at Bell Laboratories, Holmdel, NJ, USA. His current research focuses on designing and implementing power-efficient transceivers for high-speed optical communications, passive optical networks, and wireless links at optical and sub-THz frequencies.